nature communications

Article

https://doi.org/10.1038/s41467-026-73803-9

Sustainable supercritical-mechanochemical process

Received: 5 July 2025

Accepted: 20 May 2026

Published online: 28 May 2026

Check for updates

Hao Zhang, Wen Ren, Qixuan Xiang, Zhiyuan Liu, Xianglong Zhang, Yaping Zhao ✉ & Huijun Tan ✉

Mechanochemistry offers a route for converting metal oxides directly into metal organic frameworks (MOFs), ensuring maximal atomic utilization. Here, we have advanced reaction scope to the supercritical regime for establishing an integrated quasi-continuous synthesis, separation, and activation process (supercritical-mechanochemical process, SCM). Within SCM, supercritical CO_2 (SC CO_2) facilitates a spatiotemporally uniform distribution of substoichiometric cosolvent ($\eta < 0.2$ μL·mg^{-1}) across mechanochemical hot-spots, where its near-zero interfacial tension optimizes mass transfer efficiency and accelerates grinding-induced nucleation. The circulation of SC CO_2-cosolvent enhanced the ability of metastable phases to form specific topological frameworks, either through monomer-crystalline interactions or intermediate transitions. A pilot-scale facility verified a rapid production rate from an initial input of 3.5 kg to the final product within 8-hour process cycle (space-time yield of 544.29 kg·m^{-3}·d^{-1}), along with ligand and cosolvent recovery rates reaching 42.66 wt% and 89.48 wt%, respectively. Techno-economic assessment underscored substantial cost advantages over conventional solvent-based methods, positioning SCM as a sustainable and competitive approach for scalable production.

Over the past 20 years, the sustained investment in research on metal-organic frameworks (MOFs) has given rise to an extensive materials space, opening up the exciting possibility of generating tailored topological structure for a wide range of applications via a rational "crystal engineering" approach[1–8]. Despite significant academic advancements in MOFs, breakthroughs in their industrialization have not met expectations. The key limitations arise from three interlocking factors: (1) starting materials, (2) synthesis conditions, and (3) post-treatment processes[4]. The atomic utilization and cost of precursors critically determine the economic viability of scaled production[9]. Concurrently, synthesis conditions always constrain the geometry, materials, and scaling capabilities of reactors[4,10]. These factors are interrelated, for instance, scaling up solvothermal processes often encounters nonlinear heat-mass transfer across time-space dimensions, while the exclusion of anions (NO_3^-, Cl^-, or ClO_4^-) in by-products present challenges to process control and reactor layout[4,5] (Fig. 1a). Furthermore, ex situ and intermittent post-treatment, particularly solid-liquid separation during the activation stage (solvent exchange[11] and vacuum drying) add to the process inefficiencies in the scale-up production of MOFs[12]. Among these challenges, solvent management has emerged as a critical bottleneck in industrial translation. It is increasingly evident that our current dependence on solvents appears unsustainable since it is wasteful of fossil-derived materials (e.g., typical industry recovery rates of solvents are only 50-80%) and necessitating intricate liquid-phase redispersion-purification to acquire the products[13].

Mechanochemistry, characterized by grinding or other mechanical actions[8,13–16], has engendered reliable solid-solid reaction methodologies[17–19], which has been selected by the International Union of Pure and Applied Chemistry (IUPAC) as a technique that has the potential to contribute to a more sustainable future[20]. Friščić et al. have conducted pioneering works, focusing extensively on precursor

School of Chemistry and Chemical Engineering, Frontiers Science Center for Transformative Molecules, Shanghai Jiao Tong University, 800 Dong Chuan Road, Shanghai, PR China. ✉e-mail: ypzhao@sjtu.edu.cn; sophie93@sjtu.edu.cn

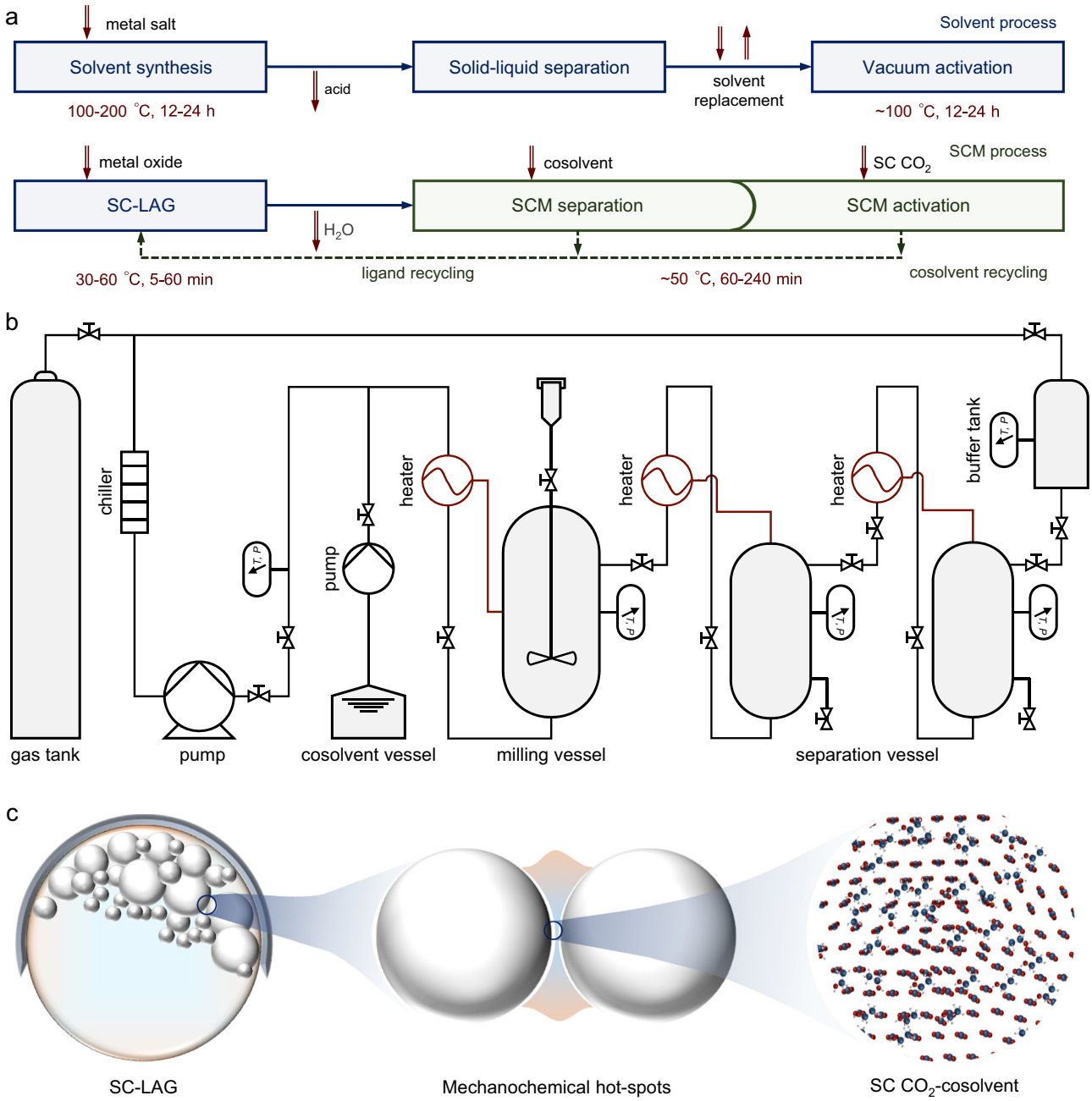

Fig. 1 | Quasi-continuous synthesis, separation, and activation of 30 g-scale ZIF-8 in SCM. a Specific comparison between the solvent-based process and SCM process for ZIF-8 production, where the solid arrows indicate material inputs and outputs, and dashed arrows denote the recovery of ligands and cosolvents in SCM. **b** The comprehensive block flow scheme for the integrated SCM process. The recovery of the ligand and cosolvent can be accomplished in the separation vessels by precisely controlling the *T* and *P* of SC CO_2. **c** Schematic illustration of SC-LAG, exemplified by a SC CO_2-EtOH mixture, constitutes a characteristic Type I mixture distinguished by complete macroscopic miscibility.

assembly[21,22], in situ intermediate observation[19,23], and interconversion of framework topologies[24,25]. The representative technique is liquid-assisted grinding[17,18] (LAG) defined by the ratio (η) of liquid volume to reactant weight. As the liquid can accelerate or enable reactions that do not proceed by neat grinding (NG), LAG offers mechanochemistry a powerful method to optimize solid-state reactions[23], particularly in the direct conversion of metal oxides (MOs) into MOFs[8,13,18]. The necessity of specifying MOs as precursors stems from their affordability, accessibility, and the generation of water as the sole by-product[4,5] (Fig. 1a). In this context, zeolitic imidazolate frameworks (ZIFs) have served as model systems due to their intriguing intermediates and topological transitions[18,19]. However, most mechanochemical syntheses of MOFs remain conducted at the gram-scale, with few attempts made to expand to larger scales. Our experiments with ZIF-8 synthesis at 30 g scale (using NG and LAG with EtOH, $\eta = 0.17\ \mu L \cdot mg^{-1}$) revealed intriguing inhomogeneity in reaction progression and solidification rates within the vessels (Supplementary Fig. 1–2, and Table 1, and Movie 1), demonstrating the limitations of substoichiometric liquid-phase in accelerating large-scale reactions. Previous reports have shown that mechanochemical synthesis involves three fundamental steps: (i) reactant diffusion via a mobile phase followed by reactive collisions, (ii) nucleation and growth of the product phase, and (iii) product separation to expose fresh reactant surface[19]. Taken together, we propose that optimal mass transfer in mechanochemical

synthesis seems to require uniform liquid-phase distribution to minimize reactant diffusion limitations. This requirement becomes particularly critical given the extremely small spatiotemporal scales characteristic of mechanochemical reactions, with the hot-spot model indicating areas of ~1 μm^2 and durations of 10^{-3}-10^{-4} s[4,13]. Under these conditions, even substoichiometric quantities of the liquid-phase may reach localized supersaturation. Consequently, identifying a more efficient solvent system that achieve both spatial uniformity and sustainable performance thus emerges as a key determinant for industrial mechanochemistry.

To address these challenges, we introduced supercritical CO_2 (SC CO_2) to achieve homogeneous dispersion of substoichiometric liquid-phase. The resulting SC CO_2-cosolvent, exemplified by a SC CO_2-EtOH, constituted a characteristic type I binary mixture[26] distinguished by complete macroscopic miscibility and polarity inversion (nonpolar-polar). Previous studies have established the mechanistic role of pure SC CO_2 in facilitating the synthesis and activation of MOFs[27–30] and other porous organic frameworks[31,32]. Central to this assertion is the understanding that SC CO_2 exhibits unparalleled dissolving capacity and permeability at the molecular scale, surpassing conventional liquid/gas phases by orders of magnitude[33–35]. From an industrial production perspective, the conditions essential to achieve the supercritical state of CO_2 are relatively modest (T_c = 31.05 °C, P_c = 7.37 MPa), and most major chemical enterprises can adequately meet these requirements (Supplementary Fig. 3 and Table 2). By precisely regulating T and P, the substoichiometric liquid-phase demonstrated the ability to form a homogeneous dispersion in SC CO_2, filling the entire vessel space and thereby facilitating more concentrated liquid-phase distribution[13] (Supplementary Fig. 4, and Table 3 and Movie 2). Furthermore, SC CO_2 serves as a recyclable working fluid, facilitating continuous solid-liquid separation and solid-phase activation[34,35]. This dual functionality enables the integration of all process steps into a single system, eliminating the redundant chemical operation units while improving production efficiency.

This work investigated the potential for industrializing MOs-MOFs using SC CO_2-cosolvent systems, integrating SC CO_2-cosolvent assisted grinding (SC-LAG) with SC CO_2-mediated separation-activation into a modularized supercritical mechanochemical (SCM) process (Fig. 1b, c and Supplementary Fig. 5). ZIF-8 was designated as a platform molecule for studying the kinetics of SCM due to the distinct crystallographic features[18,19,23,36]. However, the mechanistic understanding of general MOs-MOFs transformations via mechanochemistry remains incomplete, primarily limited by the solubility[4,5,37], M-O bonding energies[5], and complex intermediates-MOFs conversion mechanisms[21]. Thus, we have also demonstrated the unreported conversions of CuO to $Cu_3(BTC)_2$ (HKUST-1, BTC = benzene-1,3,5-tricarboxylate), as well as the more challenging ZnO to $Zn_4O(BDC)_3$ (MOF-5, BDC = benzene-1,4-dicarboxylate) at a 20 g scale using SCM. Detailed molecular dynamics (MD) simulations pointed to the homogeneous dispersion of cosolvent in SC CO_2, followed by the supersaturated aggregation near the crystalline surface of MOFs as the key to the enhanced efficiency in SCM. Furthermore, the time-resolved in situ powder X-ray diffraction (TRIS-PXRD) results emphasized that grinding products possess the potential to undergo further Oswald ripening in SC CO_2-cosolvent. By precisely regulating the state of SC CO_2 in SCM, we achieved the ligand recovery rates of 42.66 wt% from overfeed (to ensure adequate transformation of MOs) and 89.48 wt% cosolvent recovery during pilot-scale (3.5 kg) SCM production (Supplementary Fig. 6). In this context, a techno-economic analysis (TEA) emphatically underscored the robust competitive advantage of the SCM process in the large-scale production.

Results

Integrated process

The quasi-continuous synthesis, separation, and activation of ZIF-8 in SCM process was initially validated at a 30 g lab-scale (Supplementary Note 1). All the products exhibited the sodalite topology (SOD) framework ZIF-8[3,19] (Supplementary Fig. 7), with the time-dependent kinetics quantitatively confirmed by Rietveld refinement analysis (Supplementary Figs. 8–11)[19,38]. Except for SC-LAG, the other three grinding modes demonstrated kinetic profiles characterized by rapid (LAG) or slow (NG and SC CO_2-assisted grinding, SCG) sigmoidal curves associated with heterogeneous nucleation[5,19,39] (Fig. 2a). In SC-LAG, ZIF-8 exhibited pronounced reflections at the initial observation (5 min) instantaneously, with a refined ZnO weight fraction of 22.67 wt %, which further decreased to 2.71 wt% by 15 min (Supplementary Fig. 12). With the increasing grinding time, the reflection intensities tended to decrease, potentially due to grinding-induced amorphization[23,25], defect formation[40,41], or the formation of other topologies[24], as discussed later. Interestingly, while LAG demonstrated a higher initial reaction rate than SCG, it ultimately led to a lower ZnO conversion. Considering the reaction complexity and inherent constraints of ex situ characterization, particularly its inhomogeneous solidification at large scales (30 g), the ratio of the reactant and product intensities (I_{ZIF}/I_{ZnO}) was calculated to enable mechanistic (Supplementary Fig. 13). This simplified view appeared true for LAG and SCG, following a (1-x)/x law[19]. For SC-LAG, I_{ZnO}/I_{ZIF} dropped more rapidly, indicating that ZnO conversion was faster than ZIF-8 growth. Further extreme proof came from NG that the conversion of ZnO was not always accompanied by nucleation. These findings suggested that the reactivity of ZnO was not inherently linked to the nucleation and growth of ZIF-8, indicating there appeared to be a factor inhibiting this process. We attributed this behavior to the scale-induced inhomogeneous solidification, as evidenced previously that NG, LAG, and SCG exhibited slabs and even spirals of cured bodies after 5, 10, and 30 min, respectively. Ideally, a mechanochemical reaction should operate as a complex system driven by both kinetic factors (stress energy input[42]) and thermodynamic factors (system heating, reaction exotherm, and stress energy conversion). Solidification compromised the stress energy transfer from the grinding balls to the minimal energy barriers necessary for nucleation, resulting in nucleation being predominantly determined by thermodynamic constraints and slower (Supplementary Table 4). SC-LAG circumvented this limitation through SC CO_2-mediated homogeneous EtOH distribution, preventing curing and enabling rapid ZIF-8 formation into directly harvestable powder (crucial for industrialization). However, the faster kinetics produced the generation of a topological framework $Zn_2(MeIm)_2CO_3$ (CSD code HOYQAP01) first observed by Friščić et al., as a product of a further reversible carbonation of ZIF-8 in the presence of CO_2 and H_2O[24,36] (Supplementary Figs. 11, 14). We proposed that EtOH elevates the solubility of H_2O in SC CO_2, synchronously accelerating the rate of ZIF-8 nucleation and $Zn_2(MeIm)_2CO_3$ generation (SCG as a counter example, Supplementary Fig. 10). To address industrial feasibility, we incorporated an excess of 2-Methylimidazole (HMeIm, 50 wt% of the initial feed) in the subsequent separation-activation step to eliminate by-products (Supplementary Fig. 15). This adjustment effectively suppressed $Zn_2(MeIm)_2CO_3$ formation and improved product purity. The recoveries of the ligand (r_{Lig}) and cosolvent (r_{Sol}) during separation-activation were also determined to be 67.65 wt% and 85.10 wt%, respectively (Supplementary Table 5 and Supplementary Fig. 16). The relatively lower r_{Lig} primarily resulted from EtOH volatilization during depressurization. The in situ Infrared (IR) spectrum further confirmed that SC-LAG ZIF-8 maintained characteristic functional groups consistent with previous reports[43]. The spectrum featured a weak absorption band at 1565 cm^{-1} attributable to C = N stretching vibrations, along with prominent peaks at 1443 and 1353 cm^{-1} corresponding to imidazole ring stretching modes. A strong band at 421 cm^{-1} was observed that corresponded to the Zn-N stretching. (Fig. 2b and Supplementary Fig. 17). Among all the grinding modes evaluated, SC-LAG demonstrated the most complete ZnO conversion capability (weight loss of 54.77% at 600 °C), highlighting its superior performance in

https://doi.org/10.1038/s41467-026-73803-9

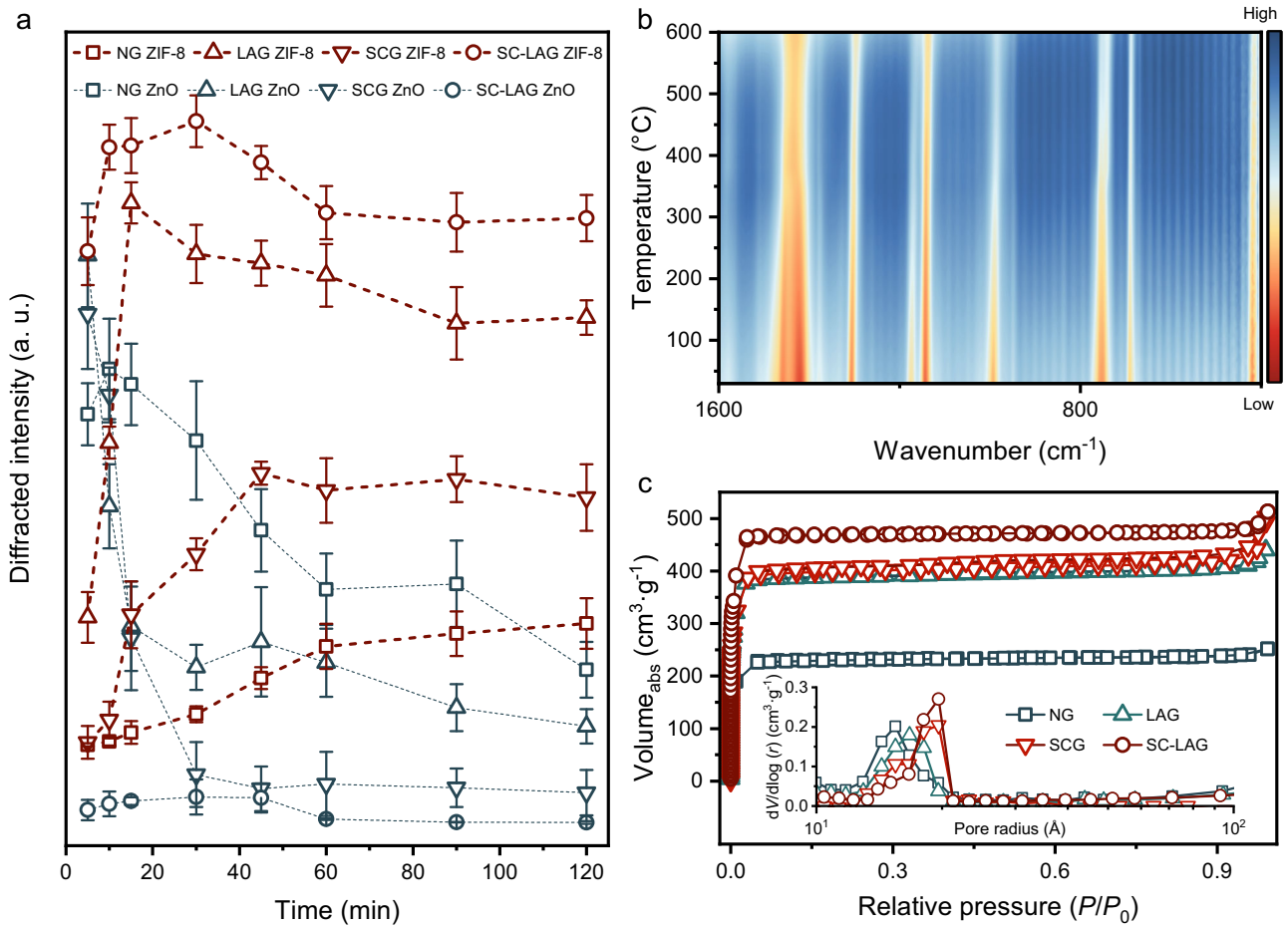

Fig. 2 | Characterizations of ZIF-8. a The conversion of ZnO to ZIF-8 using various grinding methodologies (NG, LAG, SCG, and SC-LAG) followed by separation-activation, illustrated by the changes in ZIF-8 (110) and ZnO (101) reflections. The units in (**a**) are arbitrary units (a. u.) and error bars represent the standard deviation as determined from least-squares refinement of the reflection intensities. **b** In situ IR spectrum (30–600 °C, 10 °C·min^{-1}) of SC-LAG ZIF-8. The IR intensity in (**b**) is displayed from red (low) to blue (high). **c**, N_2 adsorption-desorption isotherms of ZIF-8 produced by different grinding methodologies and the subsequent separation-activation (inset shows the pore size distribution curves). The milling configurations are consistent: grinding time (t) =120 min, fill factor (φ_{GB}) = 26.70%, ball-particle mass ratio (R_{bp}) = 15:1, rotation-to-revolution speed ratio (k) = (−2):1, η = 0.17 μL·mg^{-1} in LAG and SC-LAG with EtOH, and SC CO_2 density (ρ) =0.55 g·cm^{-3} in SCG and SC-LAG.

achieving both high yield and high-quality topological framework (Supplementary Table 6, and Fig. 18).

Another intriguing effect of eliminating by-products was the transformation of ZIF-8 crystals from amorphous to rhombic dodecahedra with exposed 12 (110) faces (Supplementary Fig. 19). Compared to the pristine rod-like ZnO, the crystals exhibited an initial size reduction (due to grinding) followed by growth. Previous reports have typically classified the excessively small crystal sizes as the metastable phase or crystalline building blocks aggregate to form a single crystal and/or iso-oriented crystals[4,5,39]. We proposed that such metastable phase formed during SC-LAG stage represented the largest crystalline domains achievable under the specific thermodynamic constraints (e.g., grinding), corresponding to a local energy minimum in the mechanochemical reaction. The subsequent separation-activation step facilitated a stable Ostwald ripening environment, enabling the metastable phase to overcome energy barriers and evolve into the thermodynamically equilibrium morphology, accompanied by a distinct crystal size progression from 127.87 ± 20.76 nm to 490.41 ± 113.87 nm (Supplementary Fig. 20). To elucidate the underlying kinetics, we conducted a segmented kinetic analysis of the SCM process (Supplementary Note 2). For SC-LAG, the time dependence of ZIF-8 (110) reflection intensity ($\alpha_t = I_0/I_{max}$) was fitted to Gualtieri model[44,45], given our earlier hypothesis that grinding preferentially enhanced nucleation over growth. Fitting the data allowed the determination of the exponential difference between the rate constants of nucleation (k_N) of 0.15 min^{-1} and crystal growth (k_G) of 1.20 × 10^{-2} min^{-1}, demonstrating that the grinding preferentially facilitates nucleation over growth (Supplementary Fig. 21–22). By contrast, in the separation-activation step, Oswald ripening may consistently favor the addition of monomers to specific crystalline surfaces, aligning more closely with the Avrami–Erofe'ev model[19,39,46]. The fitted growth rate (k_a = 1.85 × 10^{-3} min^{-1}) and Avrami exponent (n = 3.12) indicated the homogeneous growth within the supercritical system. Accompanied by the thorough growth via separation-activation, the BET specific surface area of SC-LAG ZIF-8 increased from 1309 ± 43 to 1430 ± 47 m^2·g^{-1} (Fig. 2c and Supplementary Fig. 23, Table 7), further confirming the enhanced crystallinity and pore accessibility from the defective to the final product[41].

Mechanism insight

To elucidate the intricate interplay among phases within SCM, MD simulations and density functional theory (DFT) calculations were employed to delineate the underlying mechanism. The observed variations in conformational evolutions underscored the rapid adsorption rate of small molecules onto the ZIF-8 (110) plane, as well as the localized enrichment within SC CO_2 (Fig. 3a, and Supplementary Fig. 24

https://doi.org/10.1038/s41467-026-73803-9

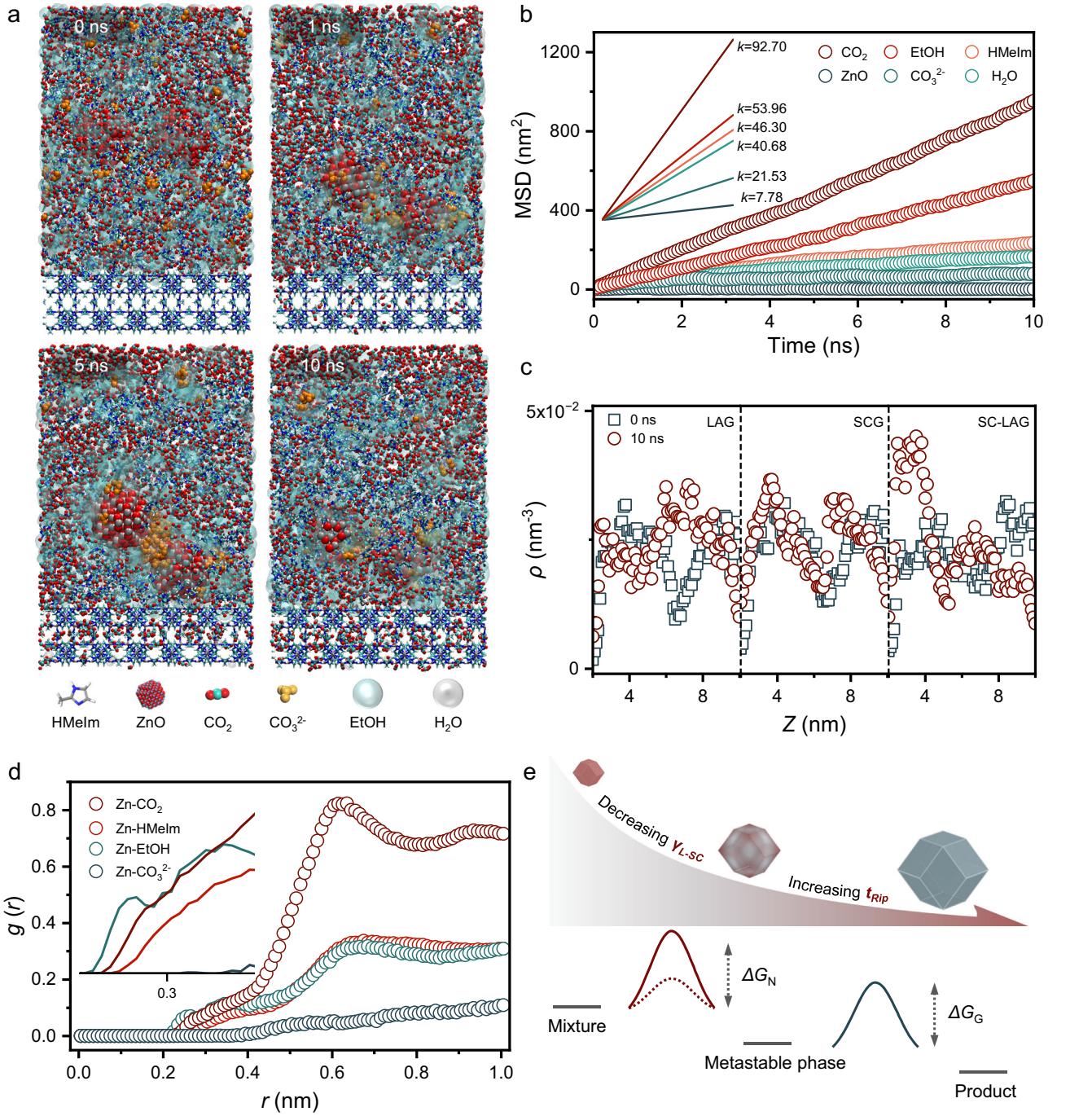

Fig. 3 | Inference of mechanism. a Evolution of the systematic conformation in SC-LAG ZIF-8 crystals (110 plane) with dimensions of 5.1 nm × 7.2 nm × 1.7 nm, applied using VMD software for trajectory visualization. The system conditions were set at 70.2 °C and 16.6 MPa. To enhance the correspondence of simulation with reality, the system was supplemented with H_2O (product) and CO_3^{2-} (generated from SC CO_2 and H_2O). **b** Mean square displacement corresponding to the components in (**a**) with the inset demonstrated the linear fit over 0-1 ns. **c** Density profiles of HMeIm in LAG, SCG and SC-LAG at 0 and 10 ns along the z-axis. **d** Radial distribution functions of the components' atoms in (**a**) (C from CO_2 and CO_3^{2-}, N from HMeIm, O from EtOH) around Zn (ZIF-8) on the surface sites, with the inset revealed the amplification at $r = 0.3$ nm. **e** Crystallization pathways of mixture (initial MOs and ligands)-metastable phase (after SC-LAG)-product (after separation-activation) in the supercritical system. The red (solid and dashed lines correspond to LAG and SC-LAG) and blue lines in (**e**) symbolized the free energy barriers for the formation of the metastable phase after grinding, and the generation of the final product through separation-activation, respectively.

and Movie 3). Further support can be derived from the mean square displacement (MSD). Apart from ZnO, the small molecules displayed typical linear-diffusive behavior[47,48], with the lowest diffusion coefficient (D) on the SC-LAG (110) plane (Fig. 3b, Supplementary Fig. 25–27 and Table 8). This preferential adsorption was further confirmed by monitoring the density distribution of HMeIm along the z-axis, which escalated by a factor of 1.33 (4.82×10^{-2} nm^{-3}) in the SC-LAG system after 10 ns around 3.5 nm, and was 2.34 and 1.09 times that of LAG and SCG, respectively (Fig. 3c). Central to this difference was the understanding that the homogeneous distribution of EtOH in SC CO_2 modulates the polarity of SC CO_2, thereby enhancing the solubility of HMeIm at mechanochemical hot-spots partially. Moreover, the deprotonation energy of HMeIm was 6.9 kcal·mol^{-1} lower in the SC-LAG system (SC CO_2-EtOH, 292.4 kcal·mol^{-1}) than in SCG (SC CO_2, 299.3 kcal·mol^{-1}),

reflecting enhanced N-H bond polarization and facilitated proton release (Supplementary Table 9–10). Radial distribution functions (RDF) analyses surrounding the (110) plane in SC-LAG further revealed that EtOH and HMeIm exhibited near-identical distribution under the relatively minor EtOH setup ($\eta = 0.17\ \mu L{\cdot}mg^{-1}$), confirming SC CO_2 effectively extracted and redistributed the HMeIm-enriched EtOH (Fig. 3d). Additionally, the RDF between various planes further revealed the preferential adsorption of small molecules on the (110) plane versus (100) plane (Supplementary Fig. 28–29). Together, these results confirmed that SC-LAG promoted targeted monomer adsorption to the specific crystal plane, driving grinding-induced nucleation and oriented crystal growth during Ostwald ripening (Supplementary Fig. 20). The sole exception arose from the anomalous distribution of CO_3^{2-} (interaction of CO_2 with H_2O) on the SC-LAG (100) plane, suggesting that reversible carbonation appeared to occur predominantly on the (100) plane. In contrast, CO_3^{2-} was nearly undetectable on the SCG (110) plane (Supplementary Fig. 28). These results corroborate our earlier hypothesis that the EtOH addition in SC CO_2 simultaneously accelerates both ZIF-8 ripening and $Zn_2(MeIm)_2CO_3$ formation, demonstrating the enhanced kinetics in SC-LAG. To further elucidate the reaction mechanism, we calculated the standard Gibbs free energy changes ($\Delta G°$) for the key steps involved (Supplementary Table 10–12). The ΔG ° value of ZIF-8 formation was found to be more than four times more exergonic than that of $Zn_2(MeIm)_2CO_3$ formation, indicating stronger thermodynamic favorability. This observation aligns with previous studies, revealing the complete crystallization of $Zn_2(MeIm)_2CO_3$ typically necessitates either prolonged aging under a humid CO_2 atmosphere or the use of carbonate precursors[36,49].

Despite the synergistic effect observed in the SC CO_2-EtOH mixture, the kinetic rate of SC-LAG did not exhibit a strictly linear dependence on cosolvent concentration. As η gradually increased to $0.60\ \mu L{\cdot}mg^{-1}$, the intensity of ZIF-8 (110) plane was observed to first rise and then decline (Supplementary Fig. 14a). As noted in our earlier discussion, surpassing the solubility limit at the supercritical point could induce the pronounced interfacial phenomenon (Supplementary Fig. 4). These interfacial effects arising between liquid-phase and supercritical-phase counteracted the advantage of low interfacial energy inherent to homogeneous SC CO_2-EtOH, impairing the mass transfer efficiency during ZIF-8 nucleation and growth. To corroborate this hypothesis, we examined MD simulations under the identical conditions with elevated η, which consistently revealed analogous microscopic phase separation (Supplementary Fig. 30a). Further potential of mean force (PMF) calculations quantified the adsorption free energy differences between the homogeneous and heterogeneous SC-LAG systems as 2.34 $kcal{\cdot}mol^{-1}$ for HMeIm, 6.16 $kcal{\cdot}mol^{-1}$ for EtOH, and 3.40 $kcal{\cdot}mol^{-1}$ for SC CO_2, respectively (Supplementary Fig. 30b–d). These results indicated that the homogeneous SC CO_2-EtOH promoted rapid interfacial adsorption and enhances mass transfer. In contrast to conventional strategies, the SCM process achieves higher efficiency in grinding-mediated nucleation and accelerates Ostwald ripening (Supplementary Fig. 31). From the preceding analysis, we cautiously propose two principles in SCM: (1) a homogeneous liquid-supercritical phase aids in mitigating the interfacial tension (γL-SC) within the mechanochemical hot-spots region, thereby maximizing the nucleation-growth efficiency, and (2) the incorporation of additional ripening process (ripening time, t_{Rip}) facilitates surmounting the free energy barriers associated with metastable phase, ultimately propelling the formation of the final product (Fig. 3e).

In situ monitoring

To further corroborate the proposed mechanism, the TRIS-PXRD[19,50] was performed for monitoring the stage of Ostwald ripening. We implemented specially designed single-crystal diamond (SCD) windows featuring a reduced thickness (0.5 mm) and enhanced pressure resistance (15 MPa), while physically decoupling the grinding and monitoring processes (Fig. 4a and Supplementary Figs. 32–35). This optimized configuration permited both an improved signal-to-background ratio and split-free Bragg peaks of samples caused by ball collisions with the windows[50,51]. All the experiments (30 gram-scale of SC-LAG) utilized identical grinding configurations. For comparison, pure SC CO_2-assisted ripening was implemented to elucidate the catalytic role of substoichiometric EtOH ($\eta = 0.17\ \mu L{\cdot}mg^{-1}$) in accelerating kinetics.

All the grinding approaches consistently yielded the SOD ZIF-8, without detectable intermediate phases confirming the direct and rapid crystallization. Plotting the time-dependent variation of the (110) reflection intensity of ZIF-8 unambiguously revealed that reactivity was improved by the EtOH additive (Fig. 4b, d). In SC-LAG (n_{Zn}: n_{MeIm} = 1: 2.1), ZIF-8 crystallization was observed near-instantaneously (2 min) with reflection intensity consistently far exceeding that of SCG throughout, demonstrating the consistent preferential-adsorption observed in the MD simulations. An anomalous structural evolution occurred at 40–50 min, characterized by a rapid decrease in ZIF-8 (110) reflection intensity following its maximum, accompanied by a rapid increase in $Zn_2(MeIm)_2CO_3$ reflection (Fig. 4e). In stark contrast, this structure was not observed in SCG. As mentioned earlier, EtOH addition inverted the polarity of SC CO_2, enabling higher solubility and mobility of H_2O molecules across the mechanochemical hot-spots. This dual effect concomitantly promoted ZIF-8 crystallization and carbonation kinetics. To eliminate the side reaction, we increased the feedstock molar ratio of SC-LAG to 1:3, leveraging Le Chatelier's principle to shift the equilibrium towards reactants. The obtained TRIS-PXRD patterns demonstrated a faster intensification of ZIF-8 (110) reflection which was distinct from the sigmoidal kinetic curve of SCG, alongside concurrent vanish of the $Zn_2(MeIm)_2CO_3$ (100) reflection (Fig. 4c, e). Moreover, A pronounced intensification of ZIF-8 (110) reflection detected during the grinding-to-ripening transition—also in agreement with the crystal size increases in ZIF-8—indicated advancing ZIF-8 crystallization under supercritical conditions (inset in Fig. 4e, Supplementary Figs. 20, 22). This highlights a discussion often underestimated in the mechanochemistry community: while precursor dissolution-coordination (nucleation) occurs through dynamic grinding, substantial crystal growth often necessitates prolonged static ripening. Building on this mechanistic insight, additional mechanochemical post-treatment may substantially contribute to the transition of metastable products into thermodynamically equilibrium morphology by overcoming energy barriers.

Universality and scalability

Utilizing the two basic principles, we executed the quasi-continuous preparation of CuO-HKUST-1 in the SCM process. Our initial attempts centered on directly LAG or SC-LAG at stoichiometric ratios, incorporating a slight excess of H_3BTC to ensure complete CuO conversion. However, the grinding product did not exhibit the anticipated blue powder, with the PXRD patterns remaining dominated by CuO reflections (Supplementary Figs. 36, 37a, 39). Recognizing the necessity of post-synthetic Ostwald ripening, we subjected the product to separation-activation after 120 min of SC-LAG. After 480 min, the product transitioned from gray-black to blue, concurrently with a pronounced increase in HKUST-1 reflection intensity (Supplementary Figs. 37b, 38, 40). Fitting the refined data to Avrami–Erofe'ev model further allowed the determination of the growth rate ($k_a = 6.51 \times 10^{-3}\ min^{-s1}$) and Avrami exponent ($n = 1.48$), demonstrating the growth during ripening, accompanied with the BET surface area increased from 92 ± 10 to $1114 \pm 92\ m^2{\cdot}g^{-1}$ (Supplementary Figs. 41–42, and Table 7). This growth in fact also involved a metastable grinding product overcoming the free energy barrier (Fig. 3e), given the absence of HKUST-1 reflections following SC-LAG. Further X-ray photoelectron spectroscopy (XPS) revealed a split peak in the Cu $2p_{3/2}$ orbital (Supplementary Fig. 43), which should have appeared at

https://doi.org/10.1038/s41467-026-73803-9

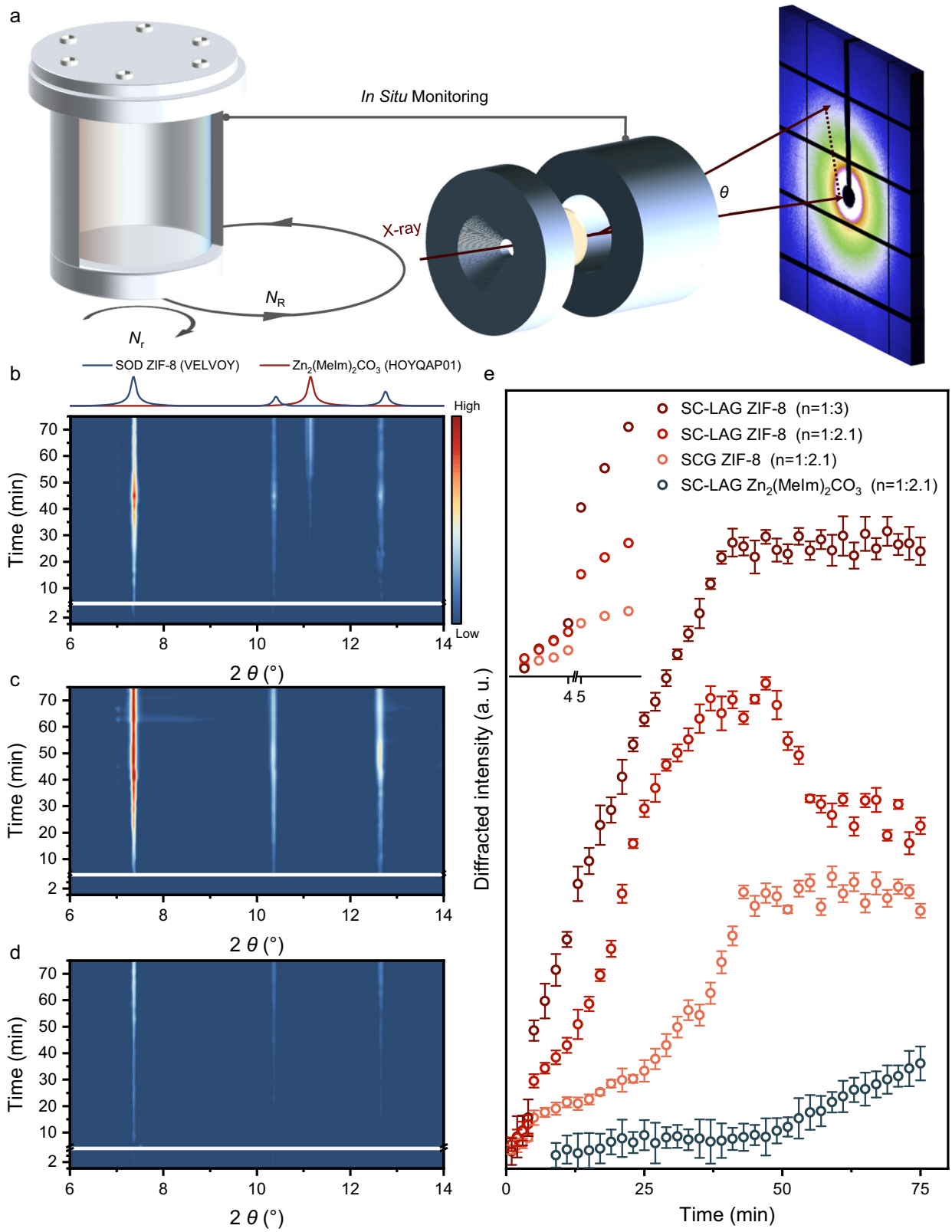

Fig. 4 | In situ monitoring for supercritical environment-enhanced Ostwald ripening. a Schematic illustration of monitoring. The black arrows represent the rotation and revolution of the planetary ball mill, whereas the red arrows indicate the direction of the X-ray beam. TRIS-PXRD diffractograms for (**b**) SC-LAG (n_{Zn}: n_{MeIm} = 1: 2.1), **c** SC-LAG under ligand-excessive conditions (n_{Zn}: n_{MeIm} = 1: 3), and (**d**) SCG (n_{Zn}: n_{MeIm} = 1: 2.1). The breakpoints in (**b**–**d**) represent the transition from direct SC-LAG monitoring to subsequent ripening under the supercritical conditions. The simulated PXRD patterns for SOD ZIF-8 (VELVOY) and $Zn_2(MeIm)_2CO_3$ (HOYQAP01) are given on top of (**b**) demonstrating the correspondence between simulated and measured diffractograms. The intensities in (**b**–**d**) are set in the identical configurations and displayed from blue (low) to red (high). **e** The time-resolved intensity changes of the ZIF-8 and $Zn_2(MeIm)_2CO_3$ reflections from (**b**–**d**) with the inset revealed the amplification from 4 to 5 min. The units in (**e**) are arbitrary units (a. u.) and error bars in (**e**) represent the standard deviation as determined from least-squares refinement of the reflection intensities according to the Pawley method.

934.1 eV (Cu^{2+}). While this split peak has been previously attributed to Cu^{+}/Cu^{0}, it may instead correspond to a more complex intermediate in this context[52,53]. Similar conclusions were also drawn from MOF-5. Compared to ZIF-8 and HKUST-1, MOF-5 features an oxo-centered secondary building unit (SBU), leading to a more intricate intermediate system, e.g., $Zn_x(BDC)_y(DMF)_z$[21,54–56]. Previous reports suggested that grinding ZnO and H_2BDC under NG tended to produce ZnBDC (CSD code DIKQET) rather than the target $Zn_4O(BDC)_3$ (CSD code SAHYIK). In SC-LAG, the high diffusivity of SC CO_2 facilitated the complexation of Zn(BDC)(DMF) (CSD code DAXNOG01), being constructed from a $Zn_2(CO_2)_4(DMF)_2$ paddle-wheel SBUs connected in two dimensions by bridging BDC linkers to give a square-grid (Supplementary Figs. 44a–c, 45)[55]. Recognizing the critical role of solvent exchange-removal in achieving the desired structure[11], we initially subjected the SC-LAG product to low-boiling-point solvent (CCl_3 and THF) exchange followed by vacuum activation (Supplementary Fig. 44d). This partially converted the dimeric SBU into tetrameric SBU (but not completely), yielding an interpenetrated MOF-5 topological framework[56,57]. The SCM separation-activation process produced analogous results, with CCl_3 outperforming THF due to its lower boiling point and superior polarity compatibility with the SC CO_2-EtOH system. Optimized conditions (ripening at 100 °C for 960 min, $CHCl_3$ exchange) enabled the intermediate to overcome free energy barriers, yielding the target $Zn_4O(BDC)_3$ (Supplementary Fig. 46, 47). Fitting the refined data to Avrami–Erofe'ev model determined the growth rate of MOF-5 ($k_a = 1.02 \times 10^{-3}\,min^{-1}$) alongside Avrami exponent ($n = 1.85$), with the BET surface area extending up to $2328 \pm 183\ m^2 \cdot g^{-1}$ (Supplementary Figs. 48, 49, Table 7). In contrast to the conventional techniques, SCM process showcased the enhanced efficiency (< 960 min), affirming the potential of SC CO_2-cosolvent as a recirculating working fluid for continuous separation-activation of specific topological frameworks, reinforcing our previous assertions.

To assess the industrial potential of the SCM process, we performed pilot-scale production of ZIF-8 with a 3.5 kg feed input, providing critical evidence for the system reliability (Supplementary Fig. 6). Scaling mechanochemical processes inherently introduces nonlinear disturbances in heat and mass transfer, along with potential safety concerns[58]. Hence, structure design and process parameters require rigorous optimization to ensure reproducible production meeting quality specifications (Supplementary Note 4). A primary scaling challenge involves preventing solidification, which compromises mixing efficiency and powder flowability, thereby impairing reaction kinetics. To address this, we amplified η to $0.25\ \mu L \cdot mg^{-1}$, and simultaneously, increased the ZnO: HMeIm molar ratio to 1:2.5 to suppress $Zn_2(MeIm)_2CO_3$ formation. The reaction kinetics mirrored laboratory-scale results, achieving high ZnO conversion within 5 min (Supplementary Fig. 50a, b). Following 240 min of separation-activation (ripening), pilot-scale ZIF-8 exhibited rapid crystallinity improvement concomitant with $Zn_2(MeIm)_2CO_3$ depletion (Supplementary Fig. 22, 50c). IR spectra and thermogravimetric analysis (TGA) further revealed comparable functional groups and thermal stability between pilot-scale and laboratory-scale products (Supplementary Fig. 50d, e). For BET surface area—a critical metric for MOFs—three pilot-scale batches exhibited reproducibility with $693 \pm 27\ m^2 \cdot g^{-1}$ (pre-ripening) and $1376 \pm 25\ m^2 \cdot g^{-1}$ (post-ripening), confirming the capability of SCM separation-activation (Supplementary Fig. 50f). Morphological evolution also matched laboratory-scale trends: amorphous nanoparticles transitioned to rhombic dodecahedra upon ripening (Supplementary Fig. 50g, h). Among all the pilot cycle (synthesis, separation, and activation), SCM process achieved 42.66 wt% ligand recovery and 89.48 wt% cosolvent recovery (Supplementary Table 5). These results were in strong agreement with laboratory-scale outcomes and confirmed that the SCM process retains its robustness and scalability from gram to multi-kilogram quantities. For larger scales, such as ton-scale production, the primary bottleneck lies in scaling mechanochemical grinding processes effectively. Our future work focuses on modifying commercial multi-ton grinding systems for compatibility with SC CO_2, with particular emphasis on the dynamic sealing performance between the agitator and grinding reactor under increasing cosolvent content. Concurrently, we are assessing the feasibility of industrial synthesis for several MOFs demonstrating practical potential, such as the industrially relevant Fe-MIL-100.

TEA analysis

Building on the demonstrated reliability of the pilot-scale SCM platform, we performed a comprehensive assessment of projected annual ZIF-8 production capacity, encompassing both economic feasibility and environmental impact analyses[59–62] (Supplementary Table 13–15). Material flow mapping across the synthesis, ripening, and activation stages provided a clear visualization of input-output dynamics and consumption trends (Fig. 5a). Among all contributors to production costs, raw material input and equipment depreciation were identified as the most significant (Fig. 5b). The SCM process enabled substantial resource recovery, with 0.87 t of HMeIm and 8504 L of EtOH reclaimed annually, substantially reducing operational costs and enhancing product competitiveness. Assuming a 10-year operational period with a 10% discount rate, the net present value (NPV) of SCM was US $21.98 M, yielding a high internal rate of return (IRR) of 37.52%[63] (Fig. 5c). Sensitivity analyses indicated that profitability was strongly influenced by raw material pricing and product market value, e.g., a 10% decrease in the HMeIm cost or 10% increase in the selling price elevated the NPV to US $23.96 M and US $27.80 M, respectively (Fig. 5d and Supplementary Table 16).

To quantitatively illustrate the investment prospects of the SCM process, we conducted a comparative analysis against the conventional processes, evaluating key parameters including process cycle conditions (synthesis, separation, and activation), actual solvent consumption, and output (Supplementary Table 17). Persistent challenges of conventional process include excessively high solvent consumption and post-processing demands, which may complicate process-cycle management and wastewater treatment during scale-up. Critically, these steps have not been accounted for in existing process cycle analyses, potentially underestimating the total environmental or operational costs. The SCM process fundamentally differs by directly integrating SC CO_2-cosolvent systems with mechanochemical synthesis, thereby combining the benefits of mechanochemistry with SC CO_2's ability to enhance reaction kinetics and enable continuous separation-activation. This approach not only reduces solvent demand by orders of magnitude but also improves process efficiency, establishing a reliable paradigm for MOF manufacturing using supercritical fluid. Taking comparable solvothermal process (SP) as an example (Supplementary Table 18): the SP process exhibits substantial inefficiencies, requiring excessive solvent volumes and extended processing times due to limited throughput and prolonged separation-activation. In contrast, the SCM process demonstrated markedly lower production costs: US $0.64k·kg^{-1} for ZIF-8, US $1.05k·kg^{-1} for HKUST-1, and US $1.78k·kg^{-1} for MOF-5, respectively (Fig. 5e). Beyond economic advantages, the SCM process demonstrates superior sustainability performance through nearly complete solvent recovery, which simultaneously minimizes resource input and effectively eliminates liquid waste streams—consistent with both green chemistry principles and circular manufacturing objectives.

Discussion

In this work, we have innovated a quasi-continuous supercritical mechanochemical process that integrates synthesis, separation, and activation establishing a sustainable and scalable strategy for the conversion of MOs to MOFs. This approach expands the mechanochemical scope by incorporating SC CO_2 medium, enabling not only

https://doi.org/10.1038/s41467-026-73803-9

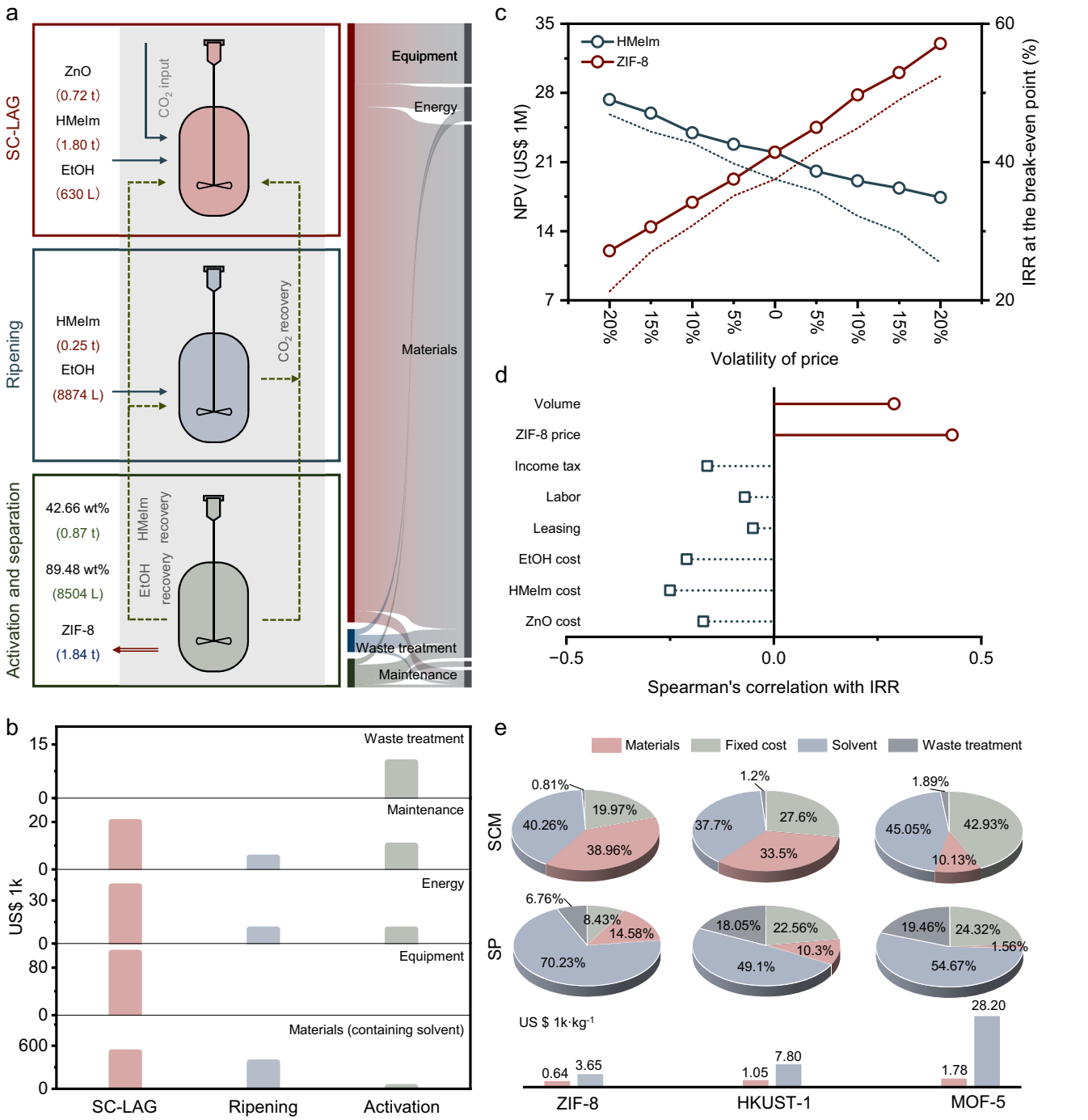

Fig. 5 | Techno-economic analysis of the SCM process. a Schematic representation of the material flow in the SCM process, along with the annual cost distribution for pilot-scale equipment. The solid arrows indicate material inputs and outputs, and dashed arrows denote the recovery of ligands and cosolvents. **b** Specific costs associated with each module of the SCM process. **c** Variations in NPV (over a 10-year operational period) and IRR (at the break-even point) in response to fluctuations in HMeIm costs and ZIF-8 selling prices. The dotted and dashed lines represent the variation in NPV and IRR, respectively. **d** Sensitivity analysis on the IRR at the break-even points, highlighting parameters with significant influence on the IRR value. e, Cost breakdowns for the SCM and SP processes in the production of ZIF-8, HKUST−1, and MOF-5. The bar chart demonstrates that the unit cost of the SCM process (red) is significantly lower than that of the SP process (blue).

efficient solid-state reactions but also growth, transformation, and activation under mild and solvent-minimized conditions. A central objective of this work is to ascertain the extensive applicability of mechanochemistry to MO-MOFs conversion, particularly for frameworks involving structurally complex intermediates. Furthermore, we emphasize that mechanochemical grinding products possess the potential to undergo further growth in supercritical system or transition into thermodynamically stable structures prior to their maturation into final products. The elevated conversion efficiency inherent to SCM might be attributed to the homogenous liquid-supercritical phase, which effectively mitigates the interfacial tension within the mechanochemical grinding hot-spots, subsequently optimizing the efficiency of cosolvent-catalyzed nucleation. Aiming for industrial applications, we amplified SCM process production and evaluated its economic viability, with costs of only 17.53% (ZIF-8), 13.46% (HKUST-1), and 6.31% (MOF-5) of the SP product (Fig. 5e). These

cost reductions, coupled with high recovery rates for both ligands and cosolvents, emphasize the alignment of SCM process with the principles of green chemistry and circular economy.

Looking ahead, two key challenges must be addressed to facilitate broader industrial adoption of the SCM methodology. First, SCM reactions involving in situ H_2O generation require careful pH management to avoid undesirable side reactions or framework degradation. Although we demonstrated the reversible carbonation to be controlled and selective, whether this process aids or hinders the generation of the specified topological frameworks, such as the selective etching of designated crystal planes, merits further exploration. Second, the scope of SCM reactions could be expanded to diverse classes of MOFs. For instance, studies are underway on industrially relevant, non-water-sensitive frameworks such as Fe-MIL-100, with findings to be reported in due course. In summary, this work advances the scope of mechanochemistry by extending it into a supercritical regime, establishing a robust and sustainable platform for transforming MOs to MOFs, fully compatible with the global initiatives in circular economy development.

Methods

Reagents and materials

All the reagents mentioned (details in Supplementary Note 1.1) were obtained from commercial vendors and used as received unless otherwise noted.

Characterizations

Powder X-ray diffraction (PXRD) patterns were examined by a Rigaku Mini Flex 600 X-ray diffractometer with Cu·K_α X-ray (λ = 1.54056 Å) in the 2θ range 10° to 50° (step 0.02°, 10 °·min^{-1}). To ensure the comparability of the diffracted intensity, the sample mass error was controlled to 200 ± 20 mg for each PXRD test and the sample was performed using a standard sample stage (loading slot of about 20 × 20 × 0.5 mm). In situ IR spectra were recorded on a Nicolet iS50 spectrometer (30–600 °C, 10 °C·min^{-1}). TGA data were effectuated with a simultaneous thermal analyser model Q600 of TA Instruments (N^2 atmosphere, 30–600 °C, 10 °C·min^{-1}). BET surface area and porous structure were analyzed using a surface aperture adsorption instrument ASAP2460 (N_2 adsorption-desorption). Before testing, the samples were degassed at 80 °C for 12 h. Ultraviolet-visible (UV-Vis) absorption spectra of the ligands were measured using a Perkins Elmer UV-Vis spectrophotometer (Lambda 750). XPS spectra of samples were analyzed using a Kratos AXIS Ultra DLD. The morphologies of samples were investigated by field-emission scanning electron microscopy (FESEM, Nova NanoSEM 450 30 kV), transmission electron microscopy (TEM, JEM-2100, 200 kV), and high-resolution TEM (HRTEM, Talos F200X G2, 200 kV). For FESEM imaging, dried samples were coated on conductive tape. For TEM and HRTEM imaging, samples were dispersed in ethanol, drop-cast onto ultrathin carbon films, and dried prior to analysis. The particle size distributions were measured and analyzed using ImageJ (1.54 d) software.

SCM experiments

SCM synthesis: As a typical lab-scale (~ 30 g) SCG experiment of ZIF-8 with φ_{GB} = 26.70%, ρ = 0.55 g·cm^{-3}, R_{bp} ≈ 15:1, and k = (-2):1, 9.80 g of ZnO (0.12 mol), 21.35 g of HMeIm (0.26 mol) and 420 g of ZrO_2 balls with different diameters were loaded into high-pressure vessel (mass ratio of 5–15 mm balls was set to 10: 35: 30: 20: 5.). Then a 5–10 min vacuum pumping process was usually necessary to make the vessel close to vacuum. About 140 g of CO_2 at 30 °C was fed into the vessel and then grinding was conducted at N_r = 450 rpm. Before grinding, the temperature of the chamber was set at 45 °C (hold for 15 min) to achieve a supercritical state. After the grinding time was completed, the samples were separated and preserved for further use. The steps of the SC-LAG experiment were generally similar to those of the SCG, except that 5.1 mL (η = 0.17 μL·mg^{-1}) of the cosolvent (EtOH) was added at the time of the feeding. The yield of MOFs in SCM was calculated according to the following equation:

$$Y = \frac{n \cdot m_{Pro} \cdot \omega_{MOF}}{m_{MOs}} \cdot \frac{N_{MOs}}{N_{MOF}} \quad (1)$$

Where n is the molar ratio of the MOs and MOFs in the corresponding chemical formula. m_{pro} and m_{MOs} represent the mass of the powder after SC CO_2 separation- activation and the mass of the MOs at the time of feeding, respectively. $\omega_{MOF\ i}$s the mass share of the MOFs determined by the Rietveld refinement. N_{MOs} and N_{MOF} represent the relative molecular mass of the MOs and MOFs, respectively. To further evaluate the SCM process in terms of industrial production capacity, the space-time yields (STYs) was further calculated:

$$STYs = \frac{m_{Pro} \cdot \omega_{MOF}}{V_{Ves} t_R} \quad (2)$$

Where V_{Ves} is the volume of the milling vessel and t_R represents grinding time.

SCM separation-activation: As a typical lab-scale (30 g) experiment of SC-LAG ZIF-8, the milling vessel was transferred and connected in series to the homemade system after grinding (details in Supplementary Information). Sieves with different mesh sizes (1000-5000 mesh) are installed between the separation vessels to minimize product loss. EtOH was loaded into the cosolvent vessel and carried into the milling vessel by continuously flowing SC CO_2 under constant temperature of 45 °C. The system was stabilized for 15–30 min after reaching 15 MPa to ensure solubility equilibrium. Subsequently, the valve of the separation vessel was opened to initiate the separation of ligand (HMeIm) at a SC CO_2 mass flow rate of 24 g·min^{-1}, under a system pressure of 15 MPa and a temperature of 45 °C. Ligand together with cosolvent was collected from the bottom of separation vessel every 5 min until no white solids precipitated. The activation of ZIF-8 (i.e., the recovery of cosolvent EtOH) commenced immediately after the separation process, at which point the valve of the cosolvent vessel was closed to permit pure SC CO_2 circulation within the system. The system was maintained at 12 MPa and 45 °C to initiate the activation of ZIF-8 (also the recovery of EtOH) at a SC CO_2 mass flow rate of 12 g·min^{-1} for ~15–30 min. The activated ZIF-8 was subsequently recovered and stored for future use. It is imperative to note that for pathways requiring the inhibition of by-products or transformation intermediates via Oswald ripening, the immediate ripening is conducted post-grinding. Upon completion, the sequential separation and recovery of the ligand and cosolvent commences. The activation and separation steps in SCG remained consistent, while NG and LAG utilized conventional centrifugal separation and vacuum activation (100 °C for 12 h). The recovery of ligand and cosolvent were calculated according to the following equations:

$$r_{Lig} = \frac{c_{Lig} \cdot v_{Sol}}{M_{Lig}(1 - n\frac{m_{Pro} \cdot Y}{M_{MOF}})} \quad (3)$$

$$r_{Sol} = \frac{m_{Sol}^{*} - c_{Lig} \cdot v_{Sol}}{m_{Sol}} \quad (4)$$

Where c_{Sol} is the concentration of ligand in the recovered cosolvent, as detected by UV spectroscopy. m_{Sol}^{*} and m_{Sol} are the mass of the recovered cosolvent and total input cosolvent, respectively. M_{Lig} is the relative molecular mass of the ligand.

Kinetic analysis

The Gualtieri model[44,45] Avrami–Erofe'ev model[19,39,46] (Eq. 5) were used jointly to analyze the entire process cycle of SCM in view of the

significantly different nucleation-growth mechanisms during the grinding and separation-activation phases. The Avrami–Erofe'ev model has been widely used to evaluate the crystallization kinetics of MOFs and the Gualtieri model is well suited for evaluating solution-mediated transformation reactions and allows differentiating nucleation and crystal growth by treating them as individual processes.

$$\alpha_t = \begin{cases} \frac{1}{1+e^{-(t-a_N)/b_N}}\left[1-e^{-(k_G t)^3}\right] & t < t_{gri} \\ 1-e^{-(k_a t)^n} & t \geq t_{gri} \end{cases} \quad (5)$$

$$P_N = \frac{dN}{dt} = e^{-\left[(t-a_N)^2/2b_N{}^2\right]} \quad (6)$$

where k_G is the rate constant of crystal growth, a_N is the reciprocal of the nucleation rate constant k_N, and b_N is the variance of the nucleation probability distribution when $t < t_{gri}$. k_a and n are the crystal growth rate constant and the Avrami exponent related to the dimensionality and the crystal growth when $t \geq t_{gri}$, respectively. The expression for P_N has a Gaussian distribution of probabilities for the total number of nuclei N present at time t. More detailed calculation steps are given in the Supplementary Note 2.

Computational methods

MD simulation: To provide direct evidence of the enhanced crystallization efficiency in SCM, we conducted MD simulations on four distinct systems: LAG, SCG, and SC-LAG (110 and 100 planes). All MD simulations were performed with the Large-scale Atomic/Molecular Massively Parallel Simulator[64] (LAMMPS, 2 Aug 2023). Molecular visualization program (VMD, 2. 0. 0a7) software was applied for trajectory visualization and analysis. We constructed surface models of ZIF-8 crystals with different crystal planes (100 and 110), with dimensions of 5.1 × 7.2 × 1.7 nm. The periodic boundary conditions (PBC) in all directions were applied to simulate volumetric behavior. Different solution system boxes were established, with ZnO, HMeIm, CO_2, EtOH, H_2O and CO_3^{2-} (potentially formed from the interaction of SC CO_2 and H_2O) molecules added separately. The solution box was combined with the ZIF-8 interface model, and a 0.5 nm vacuum layer was added to prevent PBC artifacts. During the production run, a time step of 1 fs was used, with data collected every 10 ps. The system was minimized, adjusting atomic positions and cell sizes while maintaining isotropic box lengths. The SCG system was simulated at 68.6 °C and 15.0 MPa, while the SC-LAG system was at 70.2 °C and 16.6 MPa (Supplementary Note 2.2), both also for 10 ns.

DFT calculations: To further elucidate the superior performance of SC CO_2-cosolvent relative to pure SC CO_2, we conducted DFT calculations on the essential reactions along the synthetic pathway. All structures were fully optimized with the B3LYP[65] functional augmented by Grimme's D3(BJ) dispersion correction [B3LYP-D3(BJ)][66] and the def2-TZVP basis set[67], as implemented in Gaussian 16. Harmonic vibrational frequency analyses at the same level verified that all stationary points are minima (no imaginary modes) and provided thermal corrections to Gibbs free energies. More detailed steps are given in the Supplementary Note 2.3.

In situ monitoring

To demonstrate supercritical environment-enhanced Ostwald ripening in ZIF-8, we utilized TRIS-PXRD to underscore the pivotal role of mechanochemical post-treatment. At the end of the predetermined grinding period, a high-pressure milling vessel was connected to an in situ sample cell via a stainless-steel tube (Φ1 mm). Under negative pressure, the material from the milling vessel was transferred into the in situ sample cell. This transfer process—from the cessation of milling to the initiation of monitoring—was completed within 30 seconds, enabling real-time and non-contact monitoring. Then the in situ sample cell was securely positioned at the designated location on the Shanghai Synchrotron Radiation Facility BL16B1 beamline station, and the thermostat was activated at 60 °C to initiate the TRIS-PXRD analysis. More detailed steps are given in the Supplementary Note 3.

Pilot-scale production

Building on our lab-scale SCM system, we designed and constructed a pilot-scale quasi-continuous facility, capable of feeding 1-5 kg, for the synthesis, separation, and activation of MOFs. Notably, the carrier for SC-LAG was transitioned from a planetary ball mill to a stirred ball mill to facilitate quasi-continuous production. During the pilot-scale production of SCM, all aspects of the manufacturing process were tested and validated. All subsystems utilize an integrated design that allows for easy assembly and transportation. The design and manufacturing processes conform to established standards, cited as ASME Boiler and Pressure Vessel Code[68] (ASME BPVC) and Chinese industry standard[69] (GB 150-2011, Pressure vessel).

TEA assessment

The TEA of the pilot-scale SCM process and the sensitivity analysis on the internal rate of return at the break-even point were conducted. The costs of infrastructure, energy consumption, and raw materials have been thoroughly assessed, accounting for market fluctuations. Assumptions regarding the production capacity, pricing, and sales volume of SCM have been rigorously evaluated to reflect the high demand for MOFs in both Chinese and international markets, particularly in the sectors of coatings, composite materials, and energy materials. Additionally, the SCM process was compared with existing MOF processes to evaluate its economic competitiveness.

Data availability

All data generated or analyzed during this study are included in this published article (and its supplementary information files). The experimental data generated in this study have been deposited in the Figshare database under the accession code (https://doi.org/10.6084/m9.figshare.32148853). Source data are provided as a source data file. Source data are provided with this paper.

References

1. Li, H., Eddaoudi, M., O'Keeffe, M. & Yaghi, O. M. Design and synthesis of an exceptionally stable and highly porous metal-organic framework. *Nature* **402**, 276–279 (1999).
2. Chui, S. S. Y., Lo, S. M. F., Charmant, J. P. H., Orpen, A. G. & Williams, I. D. A chemically functionalizable nanoporous material $[Cu_3(TMA)_2(H_2O)_3]_n$. *Science* **283**, 1148–1150 (1999).
3. Park, K. S. et al. Exceptional chemical and thermal stability of zeolitic imidazolate frameworks. *Proc. Natl. Acad. Sci.* **103**, 10186–10191 (2006).
4. Stock, N. & Biswas, S. Synthesis of metal-organic frameworks (MOFs): routes to various MOF topologies, morphologies, and composites. *Chem. Rev.* **112**, 933–969 (2011).
5. Carpenter, B. P., Talosig, A. R., Rose, B., Di Palma, G. & Patterson, J. P. Understanding and controlling the nucleation and growth of metal-organic frameworks. *Chem. Soc. Rev.* **52**, 6918–6937 (2023).
6. Van Vleet, M. J., Weng, T., Li, X. & Schmidt, J. R. In situ, time-resolved, and mechanistic studies of metal-organic framework nucleation and growth. *Chem. Rev.* **118**, 3681–3721 (2018).
7. Lee, J. et al. Metal-organic framework materials as catalysts. *Chem. Soc. Rev.* **38**, 1450–1459 (2009).
8. Friščić, T., Mottillo, C. & Titi, H. M. Mechanochemistry for synthesis. *Angew. Chem. Int. Ed.* **59**, 1018–1029 (2019).
9. Lin, J.-B. et al. A scalable metal-organic framework as a durable physisorbent for carbon dioxide capture. *Science* **374**, 1464–1469 (2021).
10. James, S. L. & Friščić, T. Mechanochemistry. *Chem. Soc. Rev.* **42**, 7494–7496 (2013).

11. Woo, H., Devlin, A. M. & Matzger, A. J. In situ observation of solvent exchange kinetics in a MOF with coordinatively unsaturated sites. *J. Am. Chem. Soc.* **145**, 18634–18641 (2023).
12. Seo, Y.-K. et al. Large scale fluorine-free synthesis of hierarchically porous iron(III) trimesate MIL-100(Fe) with a zeolite MTN topology. *Microporous Mesoporous Mater.* **157**, 137–145 (2012).
13. James, S. L. et al. Mechanochemistry: opportunities for new and cleaner synthesis. *Chem. Soc. Rev.* **41**, 413–447 (2012).
14. Julien, P. A., Mottillo, C. & Friščić, T. Metal-organic frameworks meet scalable and sustainable synthesis. *Green. Chem.* **19**, 2729–2747 (2017).
15. Ghanem, M. A. et al. The role of polymer mechanochemistry in responsive materials and additive manufacturing. *Nat. Rev. Mater.* **6**, 84–98 (2020).
16. Martinez, V., Stolar, T., Karadeniz, B., Brekalo, I. & Užarević, K. Advancing mechanochemical synthesis by combining milling with different energy sources. *Nat. Rev. Chem.* **7**, 51–65 (2022).
17. Friščić, T., Trask, A. V., Jones, W. & Motherwell, W. D. S. Screening for inclusion compounds and systematic construction of three-component solids by liquid-assisted grinding. *Angew. Chem. Int. Ed.* **45**, 7546–7550 (2006).
18. Beldon, P. J. et al. Rapid room-temperature synthesis of zeolitic imidazolate frameworks by using mechanochemistry. *Angew. Chem. Int. Ed.* **49**, 9640–9643 (2010).
19. Friščić, T. et al. Real-time and in situ monitoring of mechanochemical milling reactions. *Nat. Chem.* **5**, 66–73 (2012).
20. Gomollón-Bel, F. Ten chemical innovations that will change our world: IUPAC identifies emerging technologies in Chemistry with potential to make our planet more sustainable. *Chem. Int.* **41**, 12–17 (2019).
21. Prochowicz, D. et al. A mechanochemical strategy for IRMOF assembly based on pre-designed oxo-zinc precursors. *Chem. Commun.* **51**, 4032–4035 (2015).
22. Karadeniz, B. et al. Benign by Design: green and scalable synthesis of zirconium UiO-metal-organic frameworks by water-assisted mechanochemistry. *ACS Sustain. Chem. Eng.* **6**, 15841–15849 (2018).
23. Katsenis, A. D. et al. In situ X-ray diffraction monitoring of a mechanochemical reaction reveals a unique topology metal-organic framework. *Nat. Commun.* **6**, 6662 (2015).
24. Brekalo, I. et al. Manometric real-time studies of the mechanochemical synthesis of zeolitic imidazolate frameworks. *Chem. Sci.* **11**, 2141–2147 (2020).
25. Bennett, T. D. et al. Facile mechanosynthesis of amorphous zeolitic imidazolate frameworks. *J. Am. Chem. Soc.* **133**, 14546–14549 (2011).
26. Fan, J. et al. Supercritical ethanol-CO_2 mixtures exhibit microscopic immiscibility: a combined study using x-ray scattering and molecular dynamics simulations. *J. Phys. Chem. Lett.* **16**, 7090–7099 (2025).
27. López-Domínguez, P. et al. Supercritical CO_2 for the synthesis of nanometric ZIF-8 and loading with hyperbranched aminopolymers. applications in CO_2 capture. *J. CO2 Util.* **18**, 147–155 (2017).
28. Marrett, J. M. et al. Supercritical carbon dioxide enables rapid, clean, and scalable conversion of a metal oxide into zeolitic metal-organic frameworks. *Cryst. Growth Des.* **18**, 3222–3228 (2018).
29. Sinnwell, M. A. et al. Kinetics and mechanisms of ZnO to ZIF-8 transformations in supercritical CO_2 revealed by in situ x-ray diffraction. *ChemSusChem* **13**, 2602–2612 (2020).
30. Nelson, A. P., Farha, O. K., Mulfort, K. L. & Hupp, J. T. Supercritical processing as a route to high internal surface areas and permanent microporosity in metal–organic framework materials. *J. Am. Chem. Soc.* **131**, 458–460 (2008).
31. Peng, L. et al. Ultra-fast single-crystal polymerization of large-sized covalent organic frameworks. *Nat. Commun.* **12**, 5077 (2021).
32. Wang, J.-X., Gu, X.-W., Lin, Y.-X., Li, B. & Qian, G. A novel hydrogen-bonded organic framework with highly permanent porosity for boosting ethane/ethylene separation. *ACS Mater. Lett.* **3**, 497–503 (2021).
33. Zhang, H. et al. Supercritical mechano-exfoliation process. *Nat. Commun.* **15**, 9329 (2024).
34. Cole-Hamilton, D. J. Homogeneous catalysis-new approaches to catalyst separation, recovery, and recycling. *Science* **299**, 1702–1706 (2003).
35. Savage, P. E., Gopalan, S., Mizan, T. I., Martino, C. J. & Brock, E. E. Reactions at supercritical conditions: applications and fundamentals. *AIChE J.* **41**, 1723–1778 (2004).
36. Mottillo, C. & Friščić, T. Carbon dioxide sensitivity of zeolitic imidazolate frameworks. *Angew. Chem. Int. Ed.* **126**, 7601–7604 (2014).
37. Tanaka, S., Kida, K., Nagaoka, T., Ota, T. & Miyake, Y. Mechanochemical dry conversion of zinc oxide to zeolitic imidazolate framework. *Chem. Commun.* **49**, 7884–7886 (2013).
38. Pawley, G. S. Unit-cell refinement from powder diffraction scans. *J. Appl. Crystallogr.* **14**, 357–361 (1981).
39. Venna, S. R., Jasinski, J. B. & Carreon, M. A. Structural evolution of zeolitic imidazolate framework-8. *J. Am. Chem. Soc.* **132**, 18030–18033 (2010).
40. Dissegna, S., Epp, K., Heinz, W. R., Kieslich, G. & Fischer, R. A. Defective metal-organic frameworks. *Adv. Mater.* **30**, 1704501 (2018).
41. Zhao, Q., Zhao, D. L. & Chung, T.-S. Thin-film nanocomposite membranes incorporated with defective ZIF-8 nanoparticles for brackish water and seawater desalination. *J. Membr. Sci.* **625**, 119158 (2021).
42. Suryanarayana, C. Mechanical alloying and milling. *Prog. Mater. Sci.* **46**, 1–184 (2001).
43. Xu, B. et al. Monitoring thermally induced structural deformation and framework decomposition of ZIF-8 through in situ temperature dependent measurements. *Phys. Chem. Chem. Phys.* **19**, 27178–27183 (2017).
44. Gualtieri, A. F. Synthesis of sodium zeolites from a natural halloysite. *Phys. Chem. Miner.* **28**, 719–728 (2001).
45. Bagi, S. D., Myerson, A. S. & Román-Leshkov, Y. Solvothermal crystallization kinetics and control of crystal size distribution of MOF-808 in a continuous flow reactor. *Cryst. Growth Des.* **21**, 6529–6536 (2021).
46. Avrami, M. Kinetics of phase change. i general theory. *J. Chem. Phys.* **7**, 1103–1112 (1939).
47. Perez-Blanco, M. E. & Maginn, E. J. Molecular dynamics simulations of carbon dioxide and water at an ionic liquid interface. *J. Phys. Chem. B* **115**, 10488–10499 (2011).
48. Perez-Blanco, M. E. & Maginn, E. J. Molecular dynamics simulations of CO_2 at an ionic liquid interface: adsorption, ordering, and interfacial crossing. *J. Phys. Chem. B* **114**, 11827–11837 (2010).
49. Gugin, N. Y., Villajos, J. A., Dautain, O., Maiwald, M. & Emmerling, F. Optimizing the green synthesis of ZIF-8 by reactive extrusion using in situ Raman spectroscopy. *ACS Sustain. Chem. Eng.* **11**, 5175–5183 (2023).
50. Lampronti, G. I. et al. Changing the game of time resolved X-ray diffraction on the mechanochemistry playground by downsizing. *Nat. Commun.* **12**, 6134 (2021).
51. Ban, V. et al. Innovative in situ ball mill for x-ray diffraction. *Anal. Chem.* **89**, 13176–13181 (2017).
52. Chen, H., Wang, L., Yang, J. & Yang, R. T. Investigation on hydrogenation of metal–organic frameworks HKUST-1, MIL-53, and ZIF-8 by hydrogen spillover. *J. Phys. Chem. C.* **117**, 7565–7576 (2013).
53. Han, S., Ciufo, R. A., Meyerson, M. L., Keitz, B. K. & Mullins, C. B. Solvent-free vacuum growth of oriented HKUST-1 thin films. *J. Mater. Chem. A* **7**, 19396–19406 (2019).
54. McKinstry, C., Cussen, E. J., Fletcher, A. J., Patwardhan, S. V. & Sefcik, J. Effect of synthesis conditions on formation pathways of

metal organic framework (MOF-5) crystals. *Cryst. Growth Des.* **13**, 5481–5486 (2013).
55. Hawxwell, S. M., Adams, H. & Brammer, L. Two-dimensional metal-organic frameworks containing linear dicarboxylates. *Acta Cryst. B* **62**, 808–814 (2006).
56. Wu, Y., Breeze, M. I., O'Hare, D. & Walton, R. I. High energy X-rays for following metal-organic framework formation: Identifying intermediates in interpenetrated MOF-5 crystallisation. *Microporous Mesoporous Mater.* **254**, 178–183 (2017).
57. Chen, B. et al. Synthesis and characterization of the interpenetrated MOF-5. *J. Mater. Chem.* **20**, 3758–3767 (2010).
58. Chakraborty, D., Yurdusen, A., Mouchaham, G., Nouar, F. & Serre, C. Large-scale production of metal-organic frameworks. *Adv. Funct. Mater.* **34**, 2309089 (2023).
59. Choi, K. R., Luo, Z. W., Kim, G. B., Xu, H. & Lee, S. Y. A microbial process for the production of benzyl acetate. *Nat. Chem. Eng.* **1**, 216–228 (2024).
60. Zhang, G. et al. Ammonia recovery from nitrate-rich wastewater using a membrane-free electrochemical system. *Nat. Sustain.* **7**, 1251–1263 (2024).
61. Severino, M. I., Gkaniatsou, E., Nouar, F., Pinto, M. L. & Serre, C. MOFs industrialization: a complete assessment of production costs. *Faraday Discuss* **231**, 326–341 (2021).
62. Severino, M. I. et al. Cost estimation of the production of MIL-100(Fe) at industrial scale from two upscaled sustainable synthesis routes. *Ind. Eng. Chem. Res.* **64**, 2708–2718 (2025).
63. Wang, W. et al. Electrochemical lithium recycling from spent batteries with electricity generation. *Nat. Sustain.* **8**, 287–296 (2025).
64. Plimpton, S. Fast parallel algorithms for short-range molecular dynamics. *J. Comput. Phys.* **117**, 1–19 (1995).
65. Becke, A. D. Density-functional thermochemistry. III. the role of exact exchange. *J. Chem. Phys.* **98**, 5648–5652 (1993).
66. Grimme, S., Ehrlich, S. & Goerigk, L. Effect of the damping function in dispersion corrected density functional theory. *J. Comput. Chem.* **32**, 1456–1465 (2011).
67. Weigend, F. & Ahlrichs, R. Balanced basis sets of split valence, triple zeta valence and quadruple zeta valence quality for H to Rn: Design and assessment of accuracy. *Phys. Chem. Chem. Phys.* **7**, 3297–3305 (2005).
68. American Society of Mechanical Engineers. Boiler and Pressure Vessel Code, Section VIII, Division 1 (BPVC.VIII.1), *Rules for Construction of Pressure Vessels*. (New York: ASME 2019).
69. China National Standardization Administration. GB 150.1-2011, *Pressure vessel (English translation)*. (BeiJing: China Standard Press 2011).

Acknowledgements

We are grateful to the Shanghai Synchrotron Radiation Facility BL16B1 beamline station (31124.02. SSRF. BL16B1), the instrument analysis center of Shanghai Jiao Tong University, and the Siyuan-1 cluster supported by the Center for High Performance Computing at Shanghai Jiao Tong University.

Author contributions

H.Z., Methodology, data curation and writing-original draft preparation. W.R., In situ monitoring design and operation. Q.X., Conceptualization and discussion. Z.L. and X.Z., Discussion. Y.Z., funding acquisition, supervision, writing, reviewing and editing of the original draft. H.T., Discussion and writing-original draft revision.

Funding

This work was supported by the Sino-Japanese Joint Research Platform on the Energy and Environmental Industry (2017YFE0127100, China) to Yaping Zhao.

Competing interests

The authors declare no competing interests.

Additional information

Supplementary information The online version contains supplementary material available at https://doi.org/10.1038/s41467-026-73803-9.

Correspondence and requests for materials should be addressed to Yaping Zhao or Huijun Tan.

Peer review information *Nature Communications* thanks Kiyoshi Matsuyama, Christian Serreand, Shaokun Tang and the other, anonymous, reviewer(s) for their contribution to the peer review of this work. A peer review file is available.